Applied Thermal Engineering 236 (2024) 121479

Contents lists available at ScienceDirect

Applied Thermal Engineering

journal homepage: www.elsevier.com/locate/apthermeng

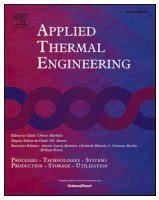

Research Paper

Experimental investigation on the effects of the geometry of microchannels based heat sinks on the flow boiling of HFE-7100

G. Marseglia [a], M.G. De Giorgi [a], D.S. Carvalho [b], P. Pontes [b], R.R. Souza [b,c], A.L.N. Moreira [b], A.S. Moita [b,d,*]

[a] University of Salento, Department of Engineering for Innovation, Via per Monteroni, Lecce 73100, Italy
[b] IN+ Center for Innovation, Technology and Policy Research, Instituto Superior Técnico, Universidade de Lisboa, Portugal
[c] Metrics, Mechanical Engineering Department, University of Minho, Campus de Azurém, 4800-058 Guimarães, Portugal
[d] CINAMIL – Military Academy Research Center, Portuguese Military Academy, Amadora, Portugal

ARTICLE INFO

Keywords:
Microchannel heat sink
Two-phase flow
Heat transfer
Boiling
Thermal performance

ABSTRACT

In this paper, nine Microchannel Heat sinks (MCHs) all with channel lengths of 20 mm and heights of 1 mm but with different aspect ratios 1.33; 2 and 4, wall thicknesses 0.25–0.75 were tested in single and two-phase flows using the HFE-7100 as the working fluid. Three different scenarios were established, changing only the inlet temperature of the fluid: ambient (18–25 °C), intermediate (38–42 °C) and near saturation (55–58 °C). In all experiments the flow at the inlet was in the laminar region with Reynolds (Re) number values ranging from 50 to 130. A thermographic camera was placed below the microchannel heat sink, to observe the cooling process during the flows. Thus, the main objective of this study is to evaluate the effects of channel geometry on both the overall heat transfer coefficient and the pressure losses. The results demonstrate that, for both single and two-phase flow, narrower channels exhibit better thermal performance but higher-pressure losses than wider channels. When maintaining channel width constant and varying thicknesses, channels with wider walls presented higher overall heat transfer coefficients and lower pressure losses.

1. Introduction

Greenhouse gas emissions are the primary cause of global warming, and their effects are already evident worldwide. Developing alternatives with lower environmental impacts and with increasing efficiency is one of the main challenges of this century. Despite extensive development, renewable sources offer sustainable solutions to mitigate the use of carbon-based fuels.

The FlightPath2050 document from EU Commission [1] highlights the importance of ensuring sustainable mobility of passengers and freight for future aircraft.

Nowadays, the electrification of aircraft propulsive systems represents an important priority because of the spreading concern about the impact of fossil fuel reserves in the aviation industry.

Different aspects such as the lower specific energy density of onboard electrical devices, and the inclusion of high-power electric devices in the aircraft producing high heat loads need optimization to allow achieving the current environmental and technical challenges [2–4].

Hybrid-electric aircraft face important thermal management issues with respect to current and conventional aircraft [5].

The importance of utilizing new architectures in thermal management system optimization is also an actual research challenge in unmanned aerial vehicles (UAVs).

Unmanned Aerial Vehicles (UAVs) have become increasingly adopted in aerospace and defense aviation applications [6]. UAVs are utilized for several purposes, integrating intelligence, surveillance, and reconnaissance military operations, network nodes, and communication relays. In fact, UAVs were the main drivers of drone applications in the US [7]. Due to the complexity and compactness of these systems, problems originate with regard to heat dissipation.

Therefore, there is a need for an efficient thermal management system that can allow to work optimally throughout the flight mission in aircraft and military sectors. In this context, the development of microelectromechanical systems (MEMS) has received increasing attention, focusing on the coupling process of solid heat conduction and fluid convection or boiling heat transfer to enhance temperature homogeneity and reduce heat accumulation in the microsystems [8].

* Corresponding author at: IN+ Center for Innovation, Technology and Policy Research, Instituto Superior Técnico, Universidade de Lisboa, Portugal.
E-mail address: anamoita@tecnico.ulisboa.pt (A.S. Moita).

https://doi.org/10.1016/j.applthermaleng.2023.121479
Received 25 May 2023; Received in revised form 1 August 2023; Accepted 1 September 2023
Available online 2 September 2023

MCHs are micro-systems that allow to transfer a high amount of heat using a small volume, thanks to a large surface area exposed to the convective and/or nucleate heat transmission processes, particularly for which have higher integrated level and operating power [9–18].

In this context, MCHSs are considered a promise for aircraft and aerospace cooling systems, because they can allow to improve thermal performance and at the same way minimize the weight [19].

Thus, the wasting of heat is still a current research issue that is leading scientists to investigate various cooling methods [20–22]. Heat transfer is strongly connected to key aspects, such as the thermophysical properties of the kind of working fluid used that affect the surface wettability and the spray-wall impact phenomenon [23].

Many researchers on MCHS have examined ways to enhance their thermal performance. One approach is to improve the design of the microchannel structures by considering their geometric features.

One of the earliest studies in the field of microchannel heat sinks was developed by Tuckerman and Pease [24] in the early 1980′s during the heyday of very-large-scale integrated (VLSI) circuits. Three different geometries were tested and the one with the better results was the narrower heat sink with 50 μm wide channels, 50 μm wide walls and water as a coolant, which exhibited a thermal resistance of 9×10^{-6} m^2K/W under a constant imposed heat flux of 790 W/cm^2. Harms et al. [25] compared a 2.5 cm wide single channel and a multiple channel system with 251 μm wide channels and 119 μm thick walls and concluded that heat transfer performance is inversely proportional to channel width. Also comparing both designs, for a given level of pressure drop, the thermal resistance of the multiple channel system was reported to be always larger than that for the single channel system. Harpole and Eninger [26] proposed a different microchannel concept with manifolds normal to the microchannel base, which guide the flow through alternating inlets and outlets. Ryu et al. [27] developed a three dimensional (3D) numerical optimization for this type of microchannel heat sinks and observed that, when comparing a manifold microchannel heat sink with a typical equivalent one, the thermal resistance was 50% less with the added benefit of significantly improving the temperature uniformity of the heated wall.

Xie et al. [28] conducted a numerical study on the influence of the geometrical proprieties of a minichannel heat sink on heat transfer and pressure drop for laminar flow. They concluded that deep and narrow channels present better thermal performances while exhibiting the highest pressure drops. Moreover, their work suggests there is an optimal value for the wall thickness of a minichannel heat sink. Raghuraman et al. [29] tested three rectangular microchannel heat sinks with three different aspect ratios (AR): 20, 30 and 46.6. The 46.6 AR microchannel heat sink required the highest pumping power, while the 20 AR microchannel heat sink presented the highest thermal resistance.

Tran et al. [30] tested one rectangular cross section channel and one circular cross section channel both with hydraulic diameters close to 2 cm and concluded that, for smaller channels, nucleation is the dominant heat transfer mechanism over convection.

Lee and Mudawar [31] studied the hydrodynamic and thermal performance of four different microchannel heat sinks with HFE-7100 as the working fluid. The effects of smaller hydraulic diameters were found to improve cooling performance by increasing mass velocity and wetted area, however for smaller channels early transition from bubbly to slug flow can arise, decreasing thermal performance.

More recently, Li and Wu [32] proposed and tested a bidirectional counter-flow microchannel heat sink with water as the working fluid and a hydraulic diameter of 400 μm. When compared to an equivalent typical microchannel heat sink, both critical heat flux and heat transfer coefficient increased between 35% and 55%, while pressure losses were significantly reduced.

The possibility to improve thermo-hydraulic efficiency considering the structure and the geometric characteristics of an interlaced MCHS is examined from [33].

Creating conditions for the occurrence of two-phase flow is also a popular strategy. Wambsganss *et al.* [34] started applying two-phase flow to microchannel heat sinks. From these two main landmarks, a great number of studies has been made to identify the best working conditions for this kind of heat sinks. However, this method comes with challenges, including energy consumption and instability caused by the presence of bubbles, making it difficult to control and describe the complex phenomena observed in the system.

Several authors, such as Lee and Mudawar [35], Li et al. [36], and Ma et al. [37], have studied different ways to optimize the efficiency of microchannel heat sinks. They have explored various approaches, including alternative geometries, surface modifications, and different working fluids.

The understanding of the boiling mechanisms involved in the saturated performance optimization for different mini-channels geometries in MCHS remains a research issue of interest for many scientists [38–40].

Zhuang et al. [41] recently investigated the flow boiling and condensation with refrigerant HFE-7100 for cooling high heat flux devices. Their results underlined the heat flux mechanism and pressure drop performances in a microchannel with an in-line circular micro-pin–fin array.

Markal et al. [42] experimentally investigated the effects of the heat and mass fluxes on the local two-phase heat transfer coefficient and the total pressure drop in a single minichannels with a defined geometry.

Recent works [43,44] analyzed the influence of the cross-sectional area ratio on flow boiling performance in MCHS, considering the two-phase pressure drop components and the heat transfer coefficients.

In this scenario, the aim of this research is to study the thermal behaviour of the working fluid considered and how different types of geometries of the MCHS would affect the heat transfer capabilities. Hence the present work is focused on two main tendencies: optimizing channel geometry and taking advantage of the contribution of the latent heat in two-phase flows. Thus, this research aims to further increase the understanding of the thermal performance and pressure losses of HFE-7100 under low velocity flows.

A novel experimental methodology is proposed to evaluate the thermal performance and pressure losses of HFE-100 in single and two-phase laminar regimes for different particular kinds of microchannel geometries.

Furthermore, an additional infrared analysis is developed during the experimental tests to better analyze the heat performance in MCHS.

The thermal behavior of HFE-7100 in single-phase and two-phase flows in the laminar regime, along with the corresponding pressure losses, have been evaluated to establish a basis for future studies aimed at determining whether the enhancements in cooling efficiency achieved through flow boiling justify the pumping power demands. To evaluate the benefits of a two-phase flow, the working fluid is HFE-7100, whose zero-ozone depletion potential and boiling point (61 °C, at ambient pressure) make it a suitable option for this work. In contrast with water, for example, HFE-7100 is a dielectric fluid, so in case of leaks or any malfunction, there is no harm caused to the electronic components of the solar power system.

Therefore, the aim is to see if the use these fluids, would increase the cooling performance of a microchannel heat exchanger and to compare the thermal behaviour of HFE-7100 single-phase and two-phase flows in the laminar regime and the corresponding pressure losses in order to develop basic and important results for future works to access if the improvements in cooling power obtained through flow boiling outweigh the pumping power requirements.

The novelty here, besides the working conditions, is the usage of a non-intrusive method, the thermographic analysis, to see the effect of the geometry when cooling a surface using flow boiling in microchannels. There is a need for design guidelines for these types of devices, as the effects of pressure drop for small channels is amplified by vapor clogging in comparison with single phase cooling.

2. Experimental methods

2.1. Experimental apparatus

For this work, nine rectangular microchannel heat sink geometries were used, all with channel lengths of 20 mm and heights of 1 mm. The chosen working fluid was HFE-7100. The main thermophysical properties of this fluid are summarized in Table 1 [45]. Three different scenarios were established, changing only the inlet temperature of the fluid: ambient (18–25 °C), intermediate (38–42 °C) and near saturation (55–58 °C).

The experimental setup used is schematically represented in Fig. 1.

The heated surface, which is being cooled by the test heat sinks is an AISI304 stainless steel sheet (87 mm × 19 mm) which was placed under the microchannel heat sinks. Two copper pieces were placed at both ends of the steel sheet and then two wires were welded to the copper.

The heat flux ($q'_0 = 5420$ W/m^2) is imposed under controlled conditions, by Joule effect, by adjusting the value of the DC current that is directly fed to the stainless-steel sheet, using a HP6274B DC power supply (2). A Harvard Apparatus Model 22 syringe (4) pumps the fluid (HFE-7100) into the microchannel heat sink (6). If required, the fluid can be heated by passing through a heat exchanger (5). Inside the channels, the fluid is flowing directly in contact with the AISI304 stainless steel sheet and is lastly stored in a reservoir (8). The current being fed to the stainless-steel is measured and monitored with a Tektronix DMM4020 multimeter (3). Inlet and outlet temperatures are measured with two type K thermocouples and are sent to a DT9828 data acquisition device (9). The pressure drop is measured with an Omega PX26-005DVdifferential pressure sensor and the data is sent to another DT9828 data acquisition device (10). Both temperature and pressure acquired values are logged using the Quick DAQ Base Package software. The working fluid, (HFE-7100) was stored and heated in a container which consists of a resistance wrapped around the container. A type K thermocouple connected to a KS 20-I PID controller takes the temperature from the working fluid inside the container and uses this information to regulate the power dissipated through the resistance (2). The fluid flows through a 700 mm long tube (with internal and external diameters of 3 mm and 4 mm, respectively) rolled around an aluminum block. The schematic of the whole container system is provided in Fig. 2.

2.1.1. Thermographic analysis

Below the microchannel heat sink (6), an Onca MWIR-InSb-320 thermographic camera (7) records the evolution of the temperature distribution around the central area of the steel sheet. Details on data reduction and calibration procedures can be found in [46,47]. The camera was positioned vertically, sustained by an aluminum support, below the microchannel heat sink. The analog to digital converter has a resolution of 14 bits so the camera assigns a value between 0 and 2^{14}-1 = 16383 analog to digital units (ADU) according to the radiation intensity. Another important aspect is the integration time, which is an adjustable parameter that allows the user to choose the exposure time for each frame. Higher integration times mean that the sensor captures more radiation, resulting in higher ADU values that can eventually saturate, for that reason it is important to choose the adequate integration time. In this work the integration time was fixed at 280 μs on the account that, based on the expected range of temperatures (40–80 °C), saturation does not occur, and the calibration software presented absolute errors lower than 1 °C. During the experimental work, the AISI 304 stainless-steel sheet (87mmx19mm) was laid down on an acrylic plate (130 mm x100mm × 5 mm) which is a material with a lower transmissivity than desired, so a small piece of sapphire glass (10 mm diameter and 3 mm height) is used to facilitate the observation of the metal sheet, as seen in Fig. 2a. Sapphire glass is electromagnetically transparent for wavelengths between 0.2 and 5.0 μm and presents a high thermal resistance [48]. The steel sheet is held down to the bottom acrylic plate with two copper pieces, one on each side. The contact between the steel sheet and the copper pieces is done through a liquid metal paste composed mainly of tin, gallium and indium (Thermal Grizzly Conductonaut) with a high electrical conductivity. Each piece has a copper wire welded to its top and was fixed to the bottom acrylic plate with two M5-0.75 internal hex screws. The microchannel heat sink is placed on top of the steel sheet with its center aligned with the sapphire glass. An acrylic plate 100 mm × 55 mm × 5 mm) was placed above, to seal the system. The top acrylic plate was fixed to the bottom one with four M5-0.75 internal hex screws. Each microchannel heat sink was perforated in the inlet and outlet plenums and the top acrylic plate had two concentric holes. In addition, the side of the steel sheet facing the thermal camera was painted black with a high temperature resistant paint to improve emissivity ($\varepsilon = 0.98$ according to the manufacturer [46]). The system represented in Fig. 3 was then fixed to a cross shaped wooden panel with a 35 mm diameter hole cut in the middle, making it possible to see the sapphire glass from below. The bottom acrylic plate was fastened to the wooden panel by two M6-0.8 set screws. Lastly, the wooden panel was placed above the aluminum structure supporting the thermographic camera and fixed with two M8-1.25 carriage bolts.

Table 1
HFE-7100 physico-chemical properties [35].

Fluid Properties at Tsat = 61 °C Value	Value
Liquid Density (kg/m3)	1400
Vapour Density (kg/m3)	9.4
Thermal Conductivity (W/m.K)	0.062
Specific Heat Capacity Liq. (kJ/kg.K)	1.26
Enthalpy of Vaporization (kJ/kg)	111.6
Kinematic Viscosity (mm2/s)	0.228

2.1.2. Microchannel systems

The microchannel heat sinks differ from each other on the width of the channels (W_c), the thickness of the walls (W_w) and the number of channels. Fig. 4 is a schematic drawing of a microchannel heat sink and the main geometric variables [49]. The nine final microchannel heat sink measurements are summarized in Table 2.

The microchannel molds were made of polylactic acid (PLA), using an Ultimaker 3 3D printer. With this equipment the minimum achievable wall thickness of a mold is 0.25 mm and this is the reason behind the channel lengths and wall thicknesses seen in Table 2. The manufacturing of the molds was done through a Fused Filament Fabrication process with a 0.25 mm diameter nozzle at 215 °C and a bed temperature of 70 °C. Each mold was then enveloped in aluminum tape and the cavity was filled with polydimethylsiloxane (PDMS). The PDMS was prepared through a mixture of Sylgard® 184 elastomer and curing agent with a mixing mass ratio of 10:1. The fluid will be in direct contact with an electrified steel sheet therefore it is beneficial that the microchannel heat sinks are electrically isolated, which is assured by the PDMS. This material is also transparent which provides optical access to the flow. Despite these advantages, PDMS has low thermal properties.

2.2. Experimental procedure

The experimental procedure is divided into two stages:

- Execution of the experimental routine consisting in the process of acquiring data regarding pressure losses, inlet and outlet fluid temperatures and steel sheet surface temperature. In this section, the inlet fluid temperatures are set for the three different experiments conducted.
- Processing and treatment of the acquired data consisting in the routine used to compute the overall heat transfer coefficients for single and two-phase flows. There are three different routines described in this section, one for each of the different ranges of inlet fluid temperatures tested.

The routine for the near saturation inlet fluid temperature experiments was repeated for the nine different geometries and followed the

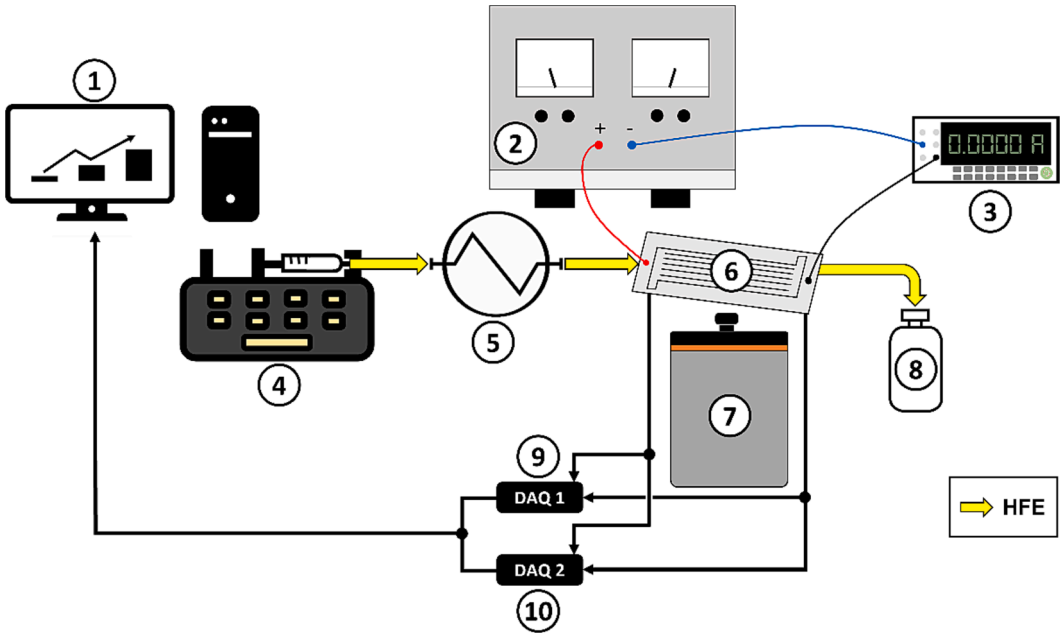

Fig. 1. Schematic of the experimental arrangement: (1) computer, (2) DC power supply, (3) multimeter, (4) syringe pump, (5) heat exchanger, (6) microchannel heat sink, (7) thermographic camera, (8) reservoir, (9) DAQ 1 and (10) DAQ 2.

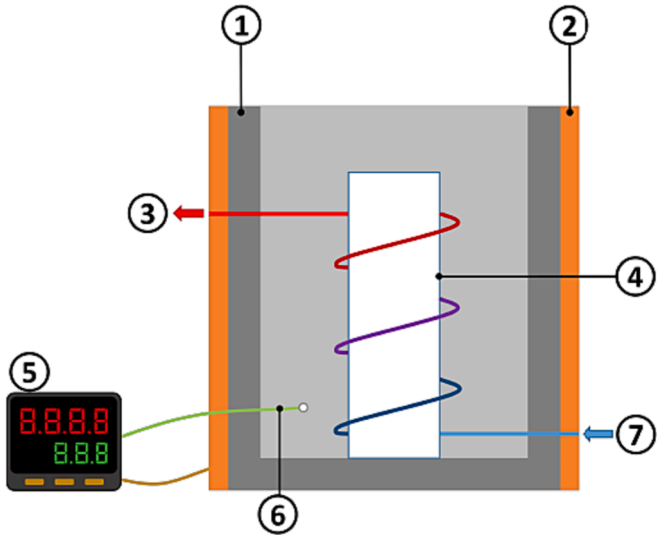

Fig. 2. Schematic of the container of the working fluid: (1) container, (2) resistance, (3) outlet, (4) aluminum block, (5) KS 20-I PID controller, (6) type K thermocouple and (7) inlet.

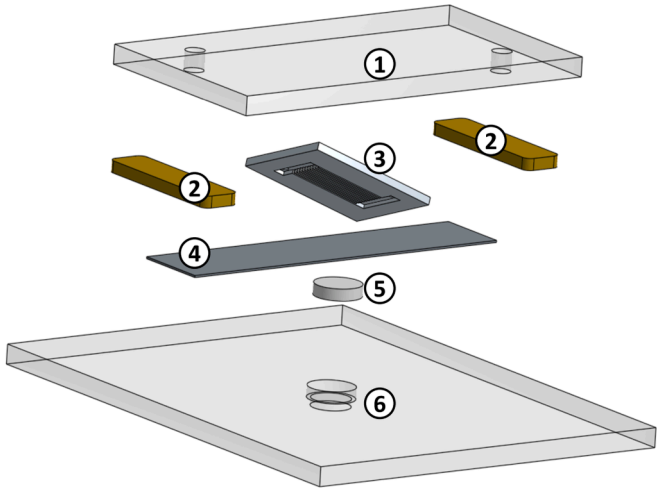

Fig. 3. Simplified explosion view of the heat sink support system: (1) upper acrylic plate, (2) copper pieces, (3) heat sink, (4) steel sheet, (5) sapphire glass and (6) bottom acrylic plate.

ensuing steps:

1. The syringe is filled with HFE-7100 at ambient temperature and the desired flow rate is set;
2. The heat exchanger resistance is turned on and the set temperature is chosen on the controller panel taking into consideration the flow rate and the desired range of inlet temperatures (55–58 °C);
3. The DC power supply is turned on with a fixed current of 8A corresponding, as previously mentioned, to a heat flux of 5420 W/m^2;
4. At this point the MATLAB routine developed in-house is initiated to keep in check the steel sheet temperature and is constantly recording at a rate of 4–6 fps;
5. When the steel sheet temperature reaches a certain temperature the syringe pump is turned on and the fluid flows to the heat exchanger. The objective is for the fluid to initially reach the steel sheet when this last one is at a temperature of 100 °C, so the temperature of the steel sheet at which the syringe pump is turned on is estimated in advance taking into account the flow rate;
6. When steady state is reached, i.e. the steel sheet temperature is practically constant, the Quick-.
7. DAQ routine is started, acquiring values of inlet and outlet temperatures and pressure drop for one minute at a 10 Hz frequency;
8. When the QuickDAQ routine finishes, the MATLAB program and the DC power supplier are turned off;
9. The steel sheet is left to cool down for five minutes and then the process is repeated.

For each microchannel heat sink five different flow rates are set (in order to get Reynolds numbers of 50, 70, 90, 110 and 130 at the entrance of each individual channel) and each flow rate is repeated five times. In

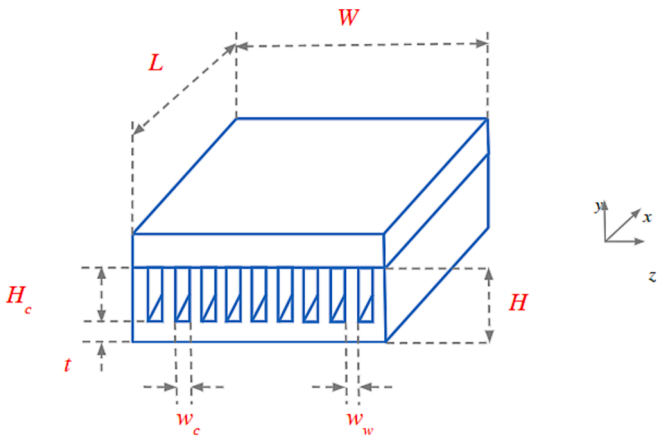

Fig. 4. Schematic of the microchannel heat sink ([38]). This figure was already in the other paper. A new one must be made.

Table 2
Microchannel heat sink geometries.

Structure	Wc (mm)	W_w (mm)	W (mm)	L (mm)	H_c (mm)	number of channels	Total cooling area (mm^2)
1	0.25	0.25	10.25	20	1	21	205
2	0.25	0.50	10.00	20	1	14	200
3	0.25	0.75	10.25	20	1	11	205
4	0.50	0.25	10.25	20	1	14	205
5	0.50	0.50	10.50	20	1	11	210
6	0.50	0.75	10.50	20	1	9	210
7	0.75	0.25	10.75	20	1	11	215
8	0.75	0.50	10.75	20	1	9	215
9	0.75	0.75	9.75	20	1	7	195

order to obtain a practically identical Reynolds number, the pump flow rate was changed, which was adjusted based on the dimensions of each channel using a reference excel spreadsheet.

The routine for the ambient inlet fluid temperature scenario was repeated for the nine different geometries and followed the ensuing steps:

1. The syringe is filled with HFE-7100 at ambient temperature and the desired flow rate is set;
2. The DC power supply is turned on with a fixed current of 8A corresponding, as previously mentioned, to a heat flux of 5420 W/m^2;
3. At this point the MATLAB routine is initiated to keep in check the steel sheet temperature and is constantly recording at a rate of 4-6fps;
4. When the steel sheet temperature reaches a certain temperature the syringe pump is turned on and the fluid flows directly to the microchannel heat sink. The objective is for the fluid to initially reach the steel sheet when this last one is at a temperature of 70 °C, so the temperature of the steel sheet at which the syringe pump is turned on is estimated in advance taking into account the flow rate;
5. When steady state is reached, i.e. the steel sheet temperature is practically constant, the Quick-DAQ routine is started, acquiring values of inlet and outlet temperatures and pressure drop for one minute at a 10 Hz frequency;
6. When the QuickDAQ routine finishes, the MATLAB program and the DC power supplier are turned off;
7. The steel sheet is left to cool down for five minutes and then the process is repeated.

Similarly to the previous scenario, there are 5 tested flow rates (in order to obtain Reynolds numbers values of 50, 70, 90, 110 and 130 at the entrance of each individual channel) and each one is repeated 5 times. Afterwards, in the interest of comparison, a similar experimental routine was repeated with geometries 2 and 9 with the fluid heated to an intermediate temperature (40 ± 2 °C). Geometry 9 was chosen because it is the geometry with the widest channel width and wall thickness. Geometry 1 is the heat sink with the narrowest channel width and wall thickness, however the walls of this geometry were damaged during the experiments in the first two scenarios, so geometry 2 was used instead.

The experimental methodology consisted in the following steps:

1. The syringe is filled with HFE-7100 at ambient temperature and the desired flow rate is set;
2. The heat exchanger resistance is turned on and the set temperature is chosen on the controller panel taking into consideration the flow rate and the desired range of inlet temperatures (38–42 °C);
3. The DC power supply is turned on with a fixed current of 8A corresponding, as previously mentioned, to a heat flux of 5420 W/m^2;
4. At this point the MATLAB routine developed by Mendes [47] is initiated to keep in check the steel sheet temperature and is constantly recording at a rate of 4-6fps;
5. When the steel sheet temperature reaches a certain temperature the syringe pump is turned on and the fluid flows to the heat exchanger. The objective is for the fluid to initially reach the steel sheet when this last one is at a temperature of 85 °C, so the temperature of the steel sheet at which the syringe pump is turned on is estimated in advance taking into account the flow rate;
6. When steady state is reached, i.e. the steel sheet temperature is practically constant, the Quick- DAQ routine is started, acquiring values of inlet and outlet temperatures and pressure drop for one minute at a 10 Hz frequency;
7. When the QuickDAQ routine finishes, the Matlab program and the DC power supplier are turned off;
8. The steel sheet is left to cool down for five minutes and then the process is repeated.

2.2.1. Data reduction

In the fully developed laminar flow region Shah and London [50] derived Eq. (1) for a rectangular channel where the channel aspect ratio (AR) is defined as the ratio between the height and the width of a channel.

$$f = \frac{24}{Re}\left(1 - 1.3553AR + 1.9467AR^2 - 1.7012AR^3 + 0.9564R^4 - 0.2537AR^5\right) \quad (1)$$

where f is the Fanning friction factor and Re is the Reynolds number. Also, the Poiseuille number is defined as the product of the Reynolds number and the Fanning friction factor and is expected to be constant for internal laminar flow. For thermally developing flow Phillips [51] compiled various values of the Nusselt number for different aspect ratios (AR) into Table 3. The values were adapted from the work of Kays [52] on thermally developing flow between two plates which is a fair approximation to make when one side of the channel is much larger than the other.

Kenning and Yan [53] modeled the surface heat flux of a thin heated plate as:

$$q'' = q_0'' + k_h\delta_h\left(\frac{\partial^2 T}{\partial x^2} + \frac{\partial^2 T}{\partial y^2}\right) - \rho_{hCp_h\delta_h}\frac{\partial T}{\partial t} \quad (2)$$

Where q_0'' is the imposed heat flux from the heater. The constants k_h, ρ_h, Cp_h and δ_h are the conductivity, density, specific heat and thickness of the heated surface. Eq. (2) can be divided into three terms: the second order spatial derivatives, the first order temporal derivative and the provided heat flux which will be considered constant. When post processing the data from the thermographic camera, the several frames are

Table 3
Typical Nusselt numbers for different aspect ratios and thermally developing laminar flow.

L/(DHRePr)	AR = 1	AR = 2	AR = 3	AR = 4
0.0001	25.20	23.70	27.00	26.70
0.0025	8.90	9.20	9.90	10.40
0.005	7.10	7.46	8.02	8.44
0.00556	6.86	7.23	7.76	8.18
0.00625	6.60	6.96	7.50	7.92
0.00714	6.32	6.68	7.22	7.63
0.00833	6.02	6.37	6.92	7.32
0.01	5.69	6.05	6.57	7.00
0.0125	5.33	5.70	6.21	6.63
0.0167	4.91	5.28	5.82	6.26
0.025	4.45	4.84	5.39	5.87
0.033	4.18	4.61	5.17	5.77
0.05	3.91	4.38	5.00	5.62
0.1	3.71	4.22	4.85	5.45
≥1	3.60	4.11	4.77	5.35

converted into matrixes with temperature values corresponding to each pixel. The temporal and spatial derivatives in equation (2) are then calculated for each pixel. These derivatives are approximated through a second-order central difference:

$$\frac{\partial^2 T}{\partial x^2} \approx \frac{T_{i,j+1,t} - 2T_{i,j,t} + T_{i,j-1,t}}{\Delta x^2} \tag{3}$$

$$\frac{\partial^2 T}{\partial y^2} \approx \frac{T_{i,j+1,t} - 2T_{i,j,t} + T_{i,j-1,t}}{\Delta y^2} \tag{4}$$

Here Δx is considered to be the pixel size calibration, changed in accordance with each test. The temporal term is approximated through a first order precision forward difference:

$$\frac{\partial T}{\partial t} \approx \frac{T_{i,j+1,t} - T_{i,j,t}}{\Delta t} \tag{5}$$

Here Δt is replaced with the time between frames (1/frames per second).

Heat transfer coefficients (h) are adapted to evaluate the thermal performance of the microchannel heat sink as a whole, like the work of Li and Wu [32]. If the fluid enters the microchannel heat sink at a temperature significantly lower than saturation, the heat transfer coefficient is calculated by eq. (6).

$$h = \frac{q''}{T_s - \frac{T_{in}+T_{out}}{2}} \tag{6}$$

Being T_s the surface temperature and T_{in}, T_{out} the liquid temperature at the entrance and exit of the heat sink. To calculate the surface temperature, the values taken from the analysis of the temperature matrixes are averaged in the studied area, similar to the procedure detailed in [47].

All the quantities obtained were averaged from 5 tests performed under similar working conditions.

For the cases where the fluid enters at temperatures close to saturation, it needs to be ascertained if the boiling point was reached in the interest area. The length of the single-phase region ($L_{s,p}$) is calculated as:

$$L_{s,p} = \frac{\dot{m} C_p (T_{sat} - T_{in})}{q'' W} \tag{7}$$

Where $\dot{m}$ is the mass flow rate, C_p is the fluid specific heat capacity, T_{sat} is the fluid saturation temperature and W is the total width of the microchannel heat sink. For the case of this work, the interest area is centered at half the length of the microchannel heat sinks, so, if $L_{s,p}$ is lower than half the length of the channel, then there was flow boiling and the heat transfer coefficient is calculated as:

$$h = \frac{q''}{T_s - T_{sat}} \tag{8}$$

If the length of the single-phase region is superior to half the length of the channel, then there was no flow boiling in the interest area and the heat transfer coefficient is calculated with eq. (9):

$$h = \frac{q''}{T_s - T_f} \tag{9}$$

where the fluid temperature T_f is given as:

$$T_f = T_{in} + \frac{q'' WL}{\dot{m} C_p} \tag{10}$$

2.2.2. Uncertainty analysis

The uncertainty values for the used equipment in the experimental work are compiled in Table 4.

The overall bias limit (B_X) of each measurement can be calculated as in [54]:

$$B_x = \left(\sum B_i^2 \right)^{1/2} \tag{11}$$

where *Bi* is the estimated error of one component that contributed to the measurement. For the pressure losses values, the overall bias limit will be affected by the pressure sensor and the syringe pump. For the heat transfer coefficient calculations, the overall bias limit will be affected by every equipment listed in Table 4, except for the pressure sensor.

2.2.3. Heat losses

Heat losses on the channel were estimated using a simplified thermal resistance model. For this purpose, the surface was considered to be in contact with two distinct materials: acrylic and sapphire and then air at ambient temperature. The equivalent thermal resistance for this system was then calculated. The details used for this calculation are included in Table 5.

3 After the thermal resistance was assessed, heat losses were estimated using the following equation:

$$q''_{loss} = \frac{T_s - T_{amb}}{R_{tot}} \bullet \frac{1}{A_{foil}} \tag{12}$$

The surface temperature during tests was measured and the heat losses estimated for each Ts. For each channel and Reynolds number, the estimated heat flux losses are displayed in Fig. 5.

3. Results and discussion

The results obtained from the experimental tests are presented and discussed in this section. Three different scenarios were tested, where the only variable was the inlet temperature: firstly, the fluid entered the microchannel heat sink at ambient temperature (between 18 °C and 25 °C), afterwards the fluid was heated up to temperatures between 55 °C and 58 °C, to evaluate the cooling potential of flow boiling. Lastly, the fluid was heated to an intermediate temperature (38 °C-42 °C) for comparison purposes of the heat sink performance, for single phase flow conditions.

Table 4
Uncertainties of the equipment used in the experimental work.

Equipment	Uncertainty
Harvard Apparatus 22 Syringe pump	±0.035%
Onca MWIR-InSb-320 Thermographic camera	±2.5%(±1°C)
Omega PX26-005DV Dif. Pressure Sensor	±1%(±0.34 kPa)
Type K Thermocouple	±0.46%(±1.5 °C)

Table 5
Properties considered to calculate heat losses.

Solid Parts			
Name	Acrylic Plate	Sapphire Glass	Units
L - Thickness	5.00E-03	3.00E-03	m
k - Thermal Conductivity	0.19	46.06	W / (m K)
A - Area	1.52E-03	1.33E-04	m^2
R = L / (k A) – Thermal Resistance	1.73E + 01	4.91E-01	K/W
Air Properties			
Name	Air Acrylic	Air Sapphire	
h - heat transfer coeficient	4	4	W / (m^2 K)
A - Area	1.52E-03	1.33E-04	m2
R = 1 / (h A) – Thermal Resistance	1.64E + 02	1.88E + 03	K/W
Tamb	21	21	°C
R total = (1/(Rac + Rair_ac) + 1/ (Rsaf + Rair_saf))$^{-1}$	1.66E + 02		K/W

3.1. Inlet ambient temperature

Pressure drop values are compiled in Fig. 6a)-c). If wall thickness is maintained constant, with the decrease in channel width there is space for more channels and, consequently, more area in contact with the fluid, which increases pressure losses. Lower widths also translate into lower hydraulic diameters so, when comparing a wider channel with a narrower channel for the same value of the Reynolds number, Re, the narrower channel will present a higher flow velocity and, consequently, higher pressure drops.

The figures also show that, maintaining wall thickness constant, with the increase in channel width promotes the decrease of pressure losses. Also, most of the geometries showcase pressure losses varying almost linearly, the Reynolds number increases. Pressure drops in ducts are proportional to the velocity squared, however, in this work, the range of Re number values evaluated is very low, so it is not possible to see the quadratic correlation between pressure losses and flow velocity.

The used pressure sensor has an uncertainty of ± 0.34 kPa which is too high to accurately measure pressure.

losses for the wider channels. Therefore, only the narrower channels are compared, as depicted in Fig. 7.

The results are overall in good agreement with the Fanning factor calculated from eq. (1). However, for lower Re number values and pressure losses, a little divergence is more evident due to the sensor sensitivity.

As for the heat transfer processes, Fig. 8a)-c) compare the experimental values of the Nusselt number, Nu, for different geometries, for inlet ambient temperature, with the same channel width.

The expectation was for heat sinks with the same aspect ratio to have similar heat transfer coefficients and heat sinks with slimmer channels to have better thermal behaviour than wider geometries.

Also, for the same geometry, the heat transfer coefficient is expected to increase slightly with the Re number. The values for the Nu number obtained from the experimental data are distant from the theoretical values. This can be partially due to the flow being thermally developing and, therefore, difficult to predict. However, this argument does not explain the fact that narrower channels do not always present the higher heat transfer coefficients. These results can further be explained by the fact that the PDMS microchannel is being compressed and, since this material is an elastometer, the aspect ratio is being changed and cannot be fully controlled. Also, the thermal conductivity of PDMS is three orders of magnitude lower than the typical values for aluminum or copper, for example. These unsuitable properties of PDMS are known. However, at this stage of the work there are clear advantages to use this material, given that it is unexpensive, easy to work with and allows for visual inspection of the flow.

3.2. Near saturation inlet temperature

The working fluid HFE-7100 was heated to temperatures between 55 and 58 °C before entering the microchannel heat sink and the main objective is to compare the heat transfer coefficients and pressure losses of single-phase and two-phase flows. Fig. 9a)-c) showcase the obtained pressure losses where the distinction between flows that reached the saturation temperature and those that did not is made.

Comparing these results with those described in section 3.1, all microchannel heat sinks present higher pressure losses, which are aggravated by the formation of air bubbles in the fluid. HFE-7100 contains up to 53% of air by volume [55] and, consequently, during the heating process the fluid releases a considerable amount of air bubbles which can perpetuate instabilities, decrease thermal behaviour and clog channels. Also, Martins [56], in a similar work, observed flow reversion which can lead to pressure fluctuations.

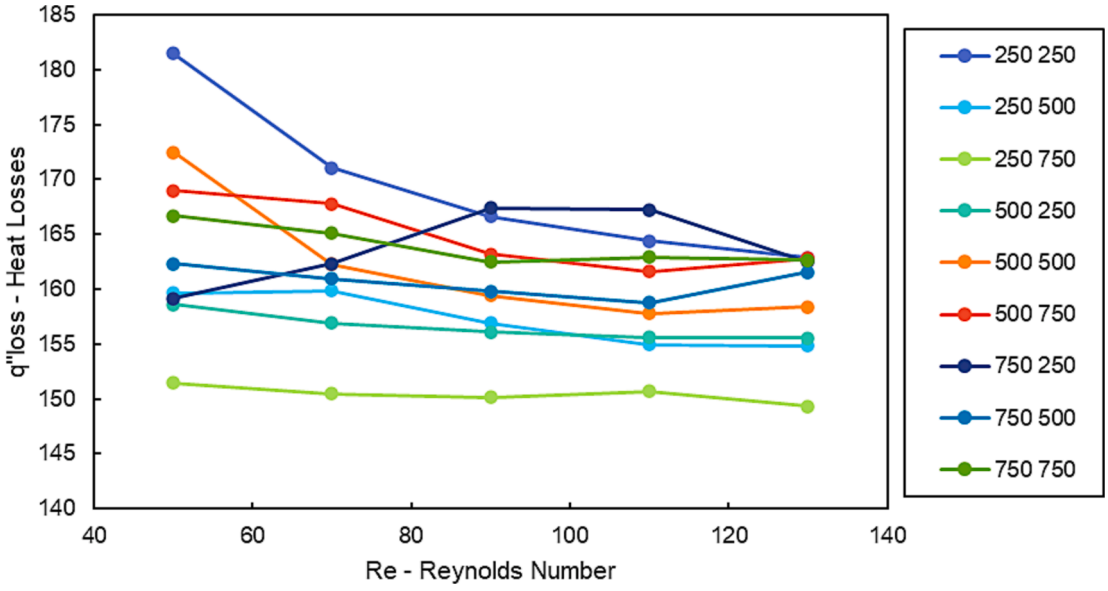

Fig. 5. Estimated heat flux losses for all tests performed.

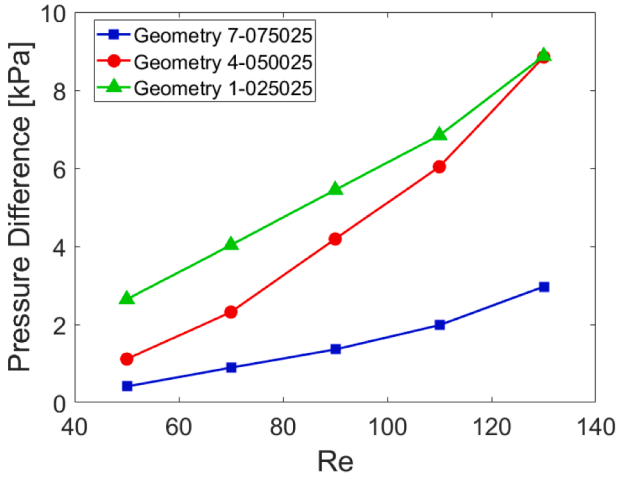

a)

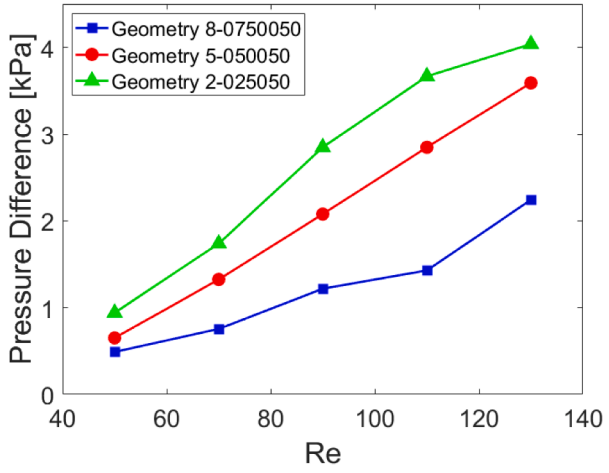

b)

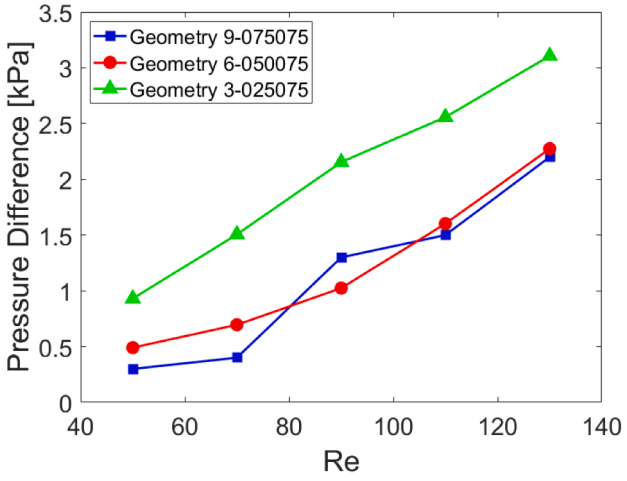

c)

Fig. 6. Pressure difference between inlet and outlet of heat sinks for different geometries: effect of the thickness of the channel walls. a) 0.25 mm thick walls, b) 0.5 mm thick walls, c) 0.75 mm thick walls.

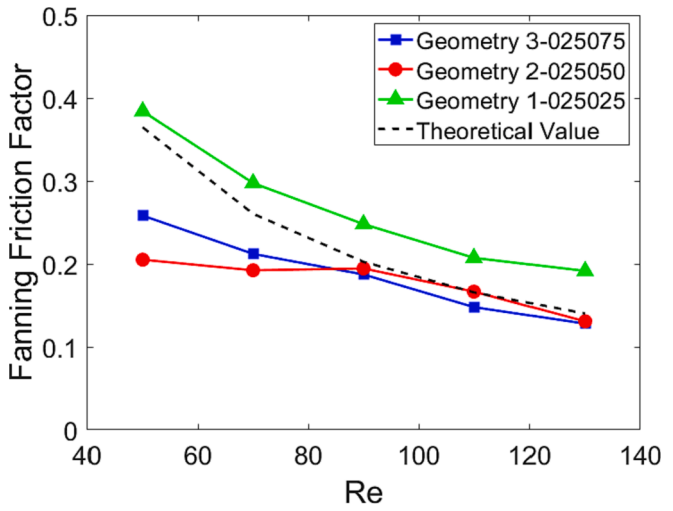

Fig. 7. Friction factor for various heat sink geometries. Comparison between experimental Fanning friction factor and theoretical values (eq.1) for geometries 1, 2 and 3.

Heat transfer coefficients are expected to be higher when compared to the values observed in section 3.1, especially when the fluid reaches boiling temperature. Thermal behaviours are again expected to be inversely proportional to channel width, however the formation of bubbles could clog the narrower channels and, consequently, worsen the thermal behaviour, as seen, for example, in the work developed by Fu et al. [57].

Fig. 10a)-c) compare heat transfer coefficients for geometries with same channel width.

The results shown in Fig. 10 show also the effect of two-phase flow on the transfer coefficient as the Reynolds number increases. Although it was expected that narrower heatsinks would present better results, what is observed is thermal instability. Due to the rapid growth of steam bubbles that form right at the entrance of the microchannels, they lead to a blockage of the passage of liquid through the channel. In other words, as the vapor title increases along the microchannels, the refrigerant flow inversion occurs, resulting in thermal instabilities, directly affecting the heat transfer performance [58–60]. This phenomenon (associated with the reverse flow of the liquid) has already been observed by other researchers in the literature and results in fluctuations in the temperature, flow and pressure of the system, which leads to the degradation of heat transfer. Or, as shown more recently [43,44], the interactions between the inertia force of the liquid and the force of the evaporation moment trigger oscillations in the inlet temperature and pressure values, causing the instabilities [61–62].

In relation to the single-phase regime, the heat transfer coefficient tends to increase as the Reynolds number increases. Although, in some cases, the acrylic plate used to keep the PDMS fixed and seal the system could have compressed the microchannel. As PDMS is a flexible elastomer, there is the possibility that small imperfections may have occurred (bent, compressed, wavy channel) in one or more of the analyzed geometries. If this happened, undulations in the channel could promote turbulence in the region, even at lower Reynolds numbers, causing instabilities and impairing the heat transfer mechanisms.

3.3. Intermediate inlet temperature

The working fluid (HFE-7100) was heated to temperatures between 38 and 42 °C, before entering the microchannel heat sink. For this ser of experiments, only geometries 2 and 9 were tested, for Re number values at the inlet of each channel of 50, 90 and 130.

In Fig. 11a)-b) pressure losses and pumping powers for geometries 2 and 9 at the intermediate temperature scenario are compared with the

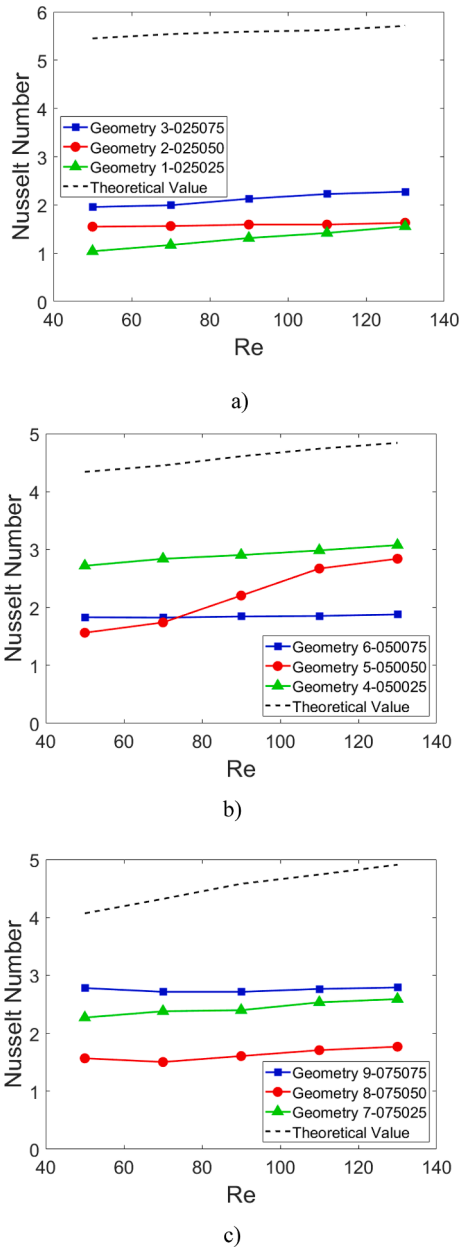

Fig. 8. Experimental Nusselt number values for geometries with variable channel widths, considering the inlet ambient temperature. a) 0.25 mm wide channels, a) 0.25 mm wide channels, b) 0.50 mm wide channels, c) 0.75 mm wide channels.

values obtained at ambient temperature and at near saturation scenarios. As expected, as the Reynolds number increases the pressure drop increases, for different initial liquid temperature levels and tested geometries. Furthermore, after the onset of nucleate boiling, i.e., when the saturation temperature of the fluid is reached, the greater the increase in pressure drop. In this condition, as the amount of vapor increases, the shear stress at the liquid–vapor interface is greater, resulting in an increase in pressure loss due to friction along the flow, as also observed [63–64]. Such behavior may even lead to reverse flow, requiring a greater pumping capacity. However, what draws the most attention in the results shown in Fig. 11a)-b) is related to the geometric effect of the outflow channels. As seen in Table 2, the two microchannels have similar total cooling areas, but differ in number of channels and width of channels (obviously). The microchannels represented by Geometry 9, present smaller values for the pressure drop for all evaluated test

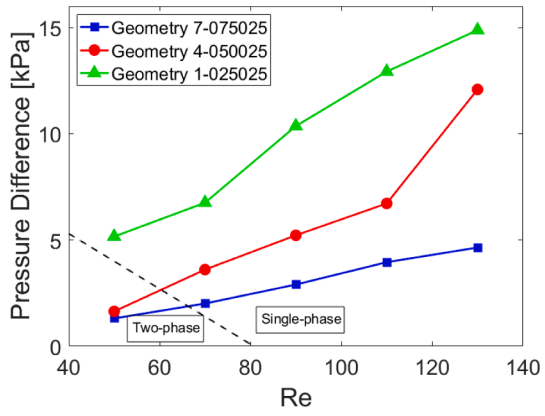

a)

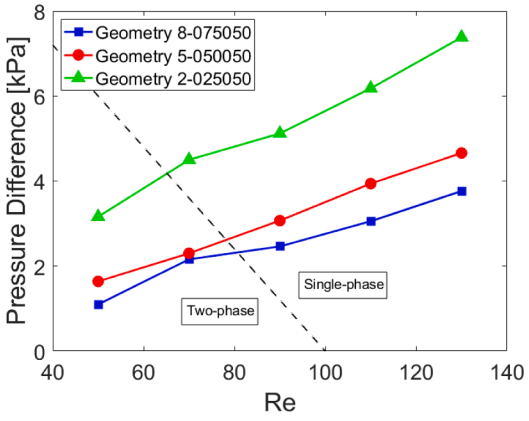

b)

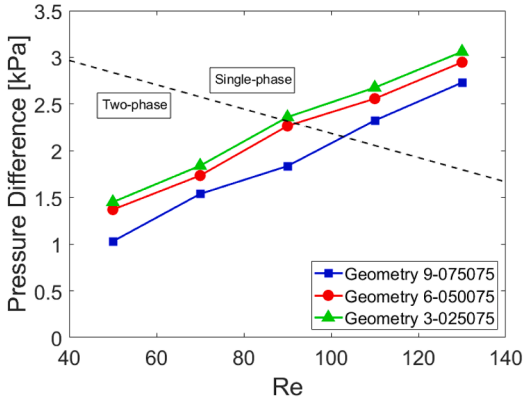

c)

Fig. 9. Pressure losses between inlet and outlet for geometries different geometries: a) Geometries1, 4 and 7, b) Geometries 2, 5 and 8, c) Geometries 3, 6 and 9.

conditions, Fig. 11b. As Geometry 9 has wider channels compared to other geometry, with more space available to flow the resistance and the liquid velocity is lower resulting in a lower pressure drop.

Fanning friction factor and Poiseuille number obtained experimentally are compared with the theoretical expectations, as depicted in Fig. 12a)-b).

As previously seen in section 3.1, the friction factor for geometry 2 is close to the theoretical one and the obtained Poiseuille number values

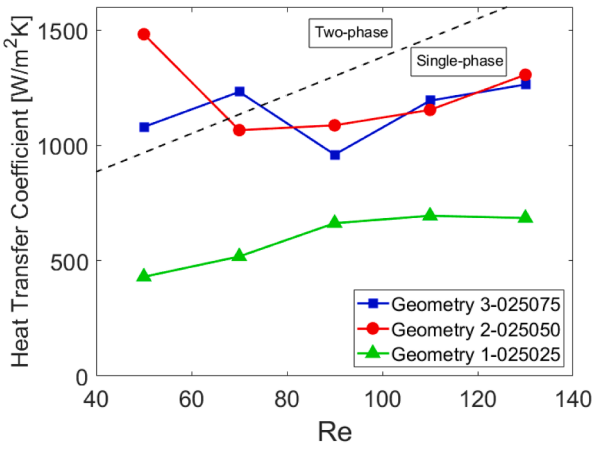

a)

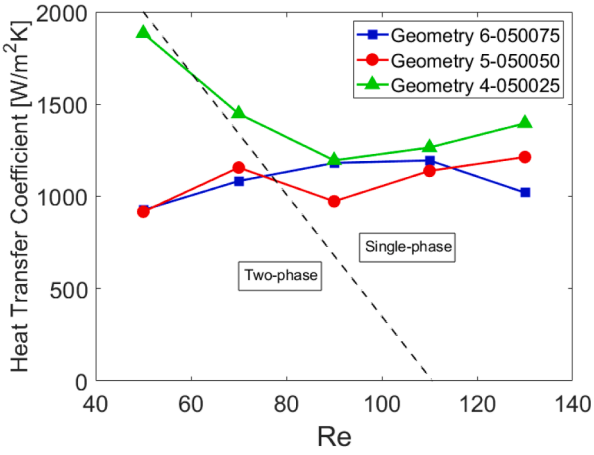

b)

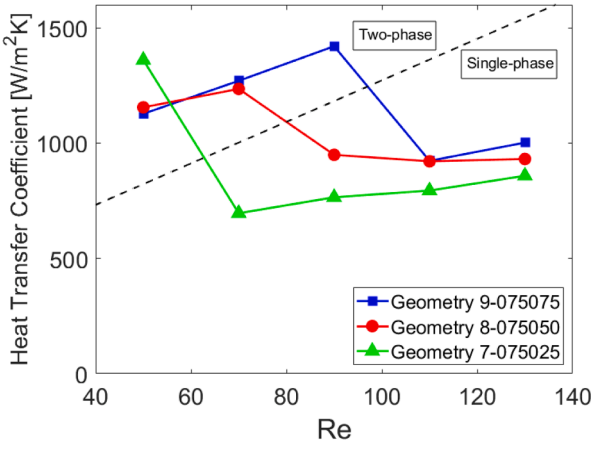

c)

Fig. 10. Heat transfer coefficients for different geometries. a) Geometries 1, 2 and 3, b) Geometries 4, 5 and 6, c) Geometries 7, 8 and 9.

diverge on average 9% from the theory. The friction factor and Poiseuille number for geometry 9 are once again very far from the theoretical values due to the pressure sensor uncertainty (±0.34 kPa).

Fig. 13a)-b) compare the Nu number values obtained experimentally

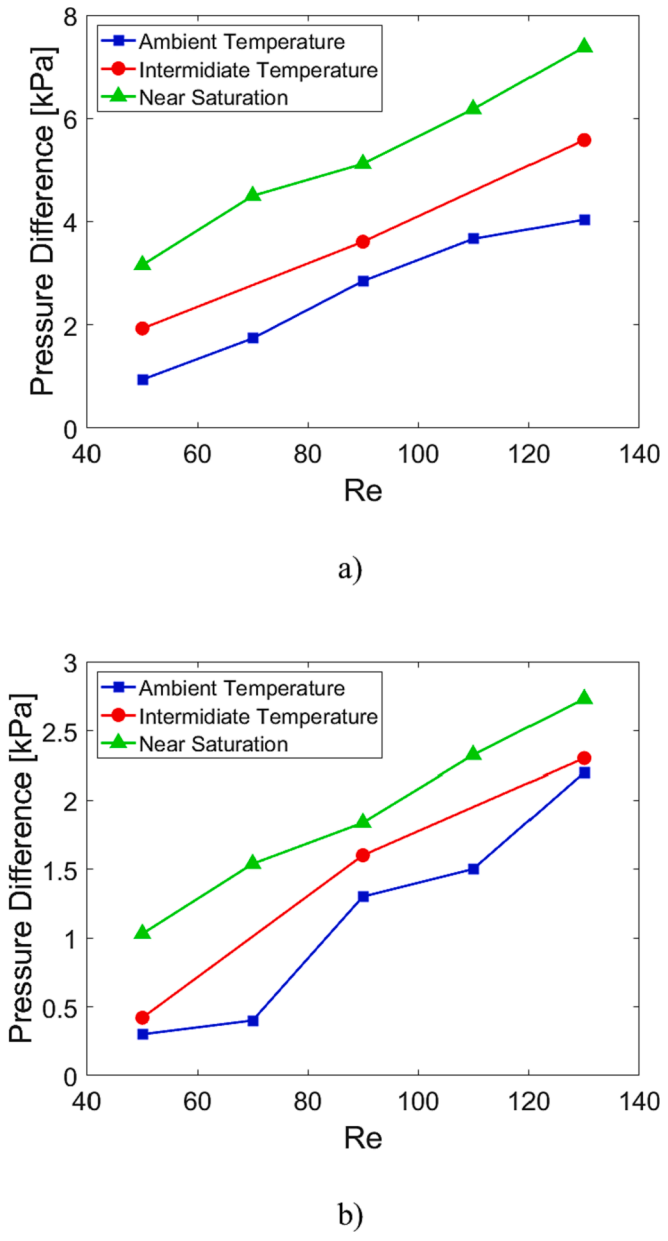

Fig. 11. Pressure difference between inlet and outlet for different geometries. Comparison for the various temperature conditions. a) Geometry 2, b) Geometry 9.

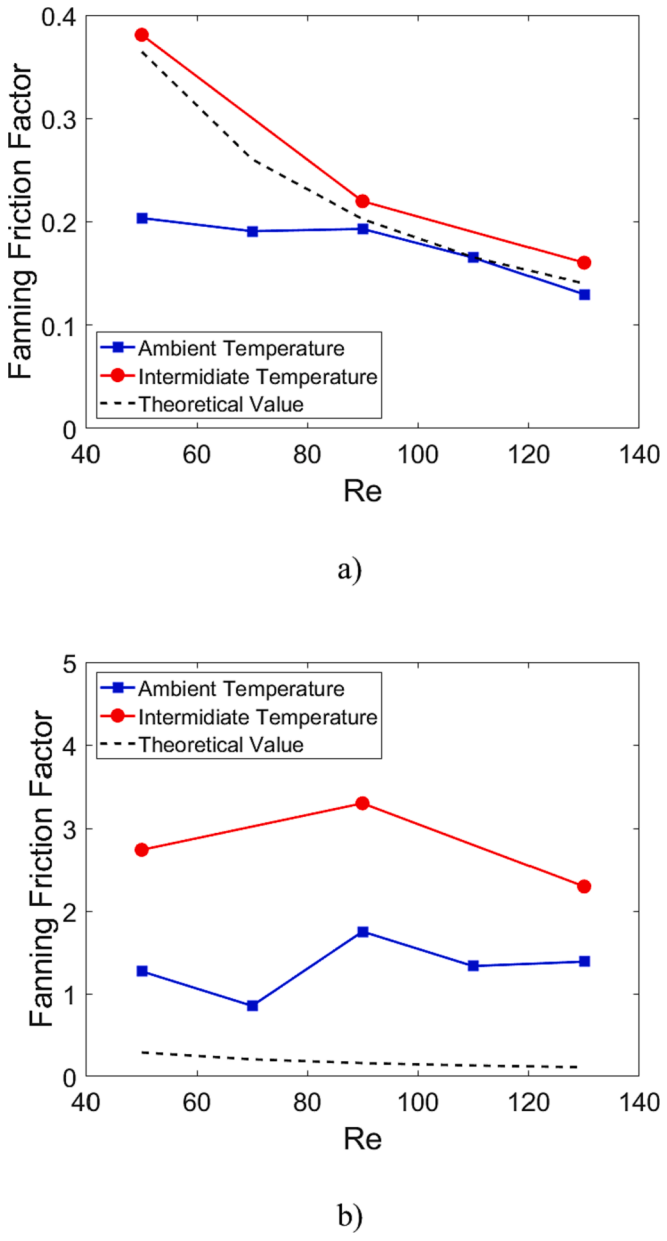

Fig. 12. Experimental Fanning friction factor compared with the expected theoretical values (eq.1) at different temperatures. a) Geometry 2, b) Geometry 9.

with those theoretically determined. Although, the Nu number values for geometry 9 are close to the theoretical values, varying on average 11%, the results are in conflict with the expected trend. As previously mentioned, it was expected that narrower geometries, as is the case of geometry 2, would present greater heat transfer. What can be concluded from this result, and consequently from the entire study presented, is that there is a dispute between the hydrodynamic and thermal effects on the flow of microchannels. In some cases, the pressure drop may play a dominant role in the flow, while the effect of forced convection is secondary. If there is a greater expenditure of energy due to pressure drop in the channels, heat transfer is impaired and there is no hydrodynamic and thermal equilibrium point. This study points out that there should be an "ideal" geometry, which may not necessarily be represented by the narrowest channels, however, to confirm this assumption, more studies are needed.

4. Conclusions

A new experimental study was conducted to evaluate the thermal performance and pressure losses of HFE-100 in single and two-phase laminar regimes. To further enhance the cooling power and overcome the pumper power requirements, flow boiling was proposed. However, the malleability of the heat sink material was identified as a major issue, and caution must be exercised in generalizing the results obtained and discussed here. Additionally, the measured pressure losses for geometries with 0.50 mm and 0.75 mm wide channels may not be entirely accurate due to the uncertainty of the differential pressure sensor.

Main conclusions can be summarized as follows:

- Keeping the thickness of the walls constant, narrowing the channels results in smaller inlet areas, leading to higher fluid velocities for the same flow rate. Consequently, narrow channel geometries are expected to exhibit higher pressure losses. The findings suggest that,

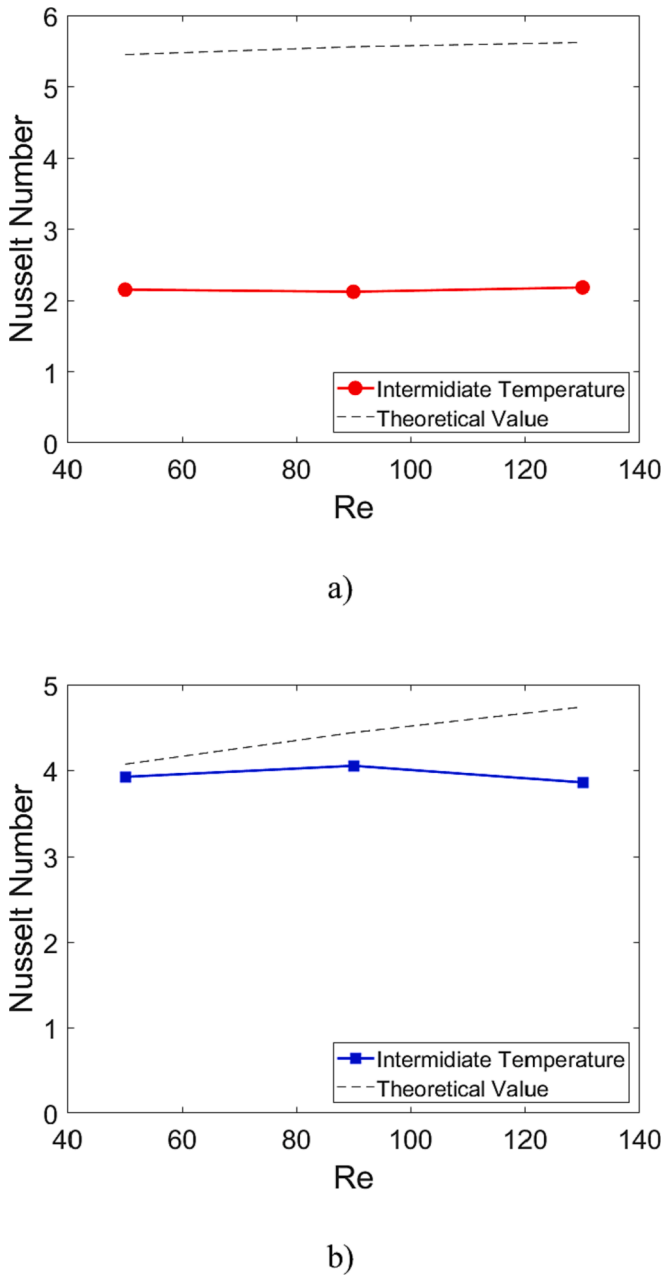

Fig. 13. Experimental Nusselt number values compared with the theoretical ones reported in Table. 5. a) Geometry 2, b) Geometry 9.

regardless of the inlet temperature, pressure losses were consistently higher for narrower geometries.

In the context of microchannel heat sinks, maintaining a constant channel width while decreasing the thickness of walls results in a higher number of channels and fluid velocities. The results obtained indicate that thinner walls lead to higher pressure losses, as expected.

- For the heated fluid scenario, it was not possible to conclude if pressure losses are significantly affected by the boiling process as the values for two-phase flow and single-phase flow often see similarly proportional increments when the flow rate is increased.
- In the ambient temperature scenario, narrower geometries were expected to have higher Nusselt number values due to their higher aspect ratio. However, the results showed a different trend with higher Nusselt numbers for wider geometries.
- In the near saturation scenario, the heat transfer coefficients in the single-phase region were higher for narrower geometries, except for geometry 1. Additionally, the results showed a decrease in the heat transfer coefficient from two-phase to single-phase flow, indicating that flow boiling at lower flow rates could result in better thermal performance with lower pumping power requirements, and hence enhance the cooling power.
- When comparing geometries with the same channel width, in the near saturation scenario, the microchannel heat sinks with 0.50 mm and 0.75 mm thick walls presented similar results, which might suggest that the same thermal behaviour can be achieved with geometries with wider walls and lower pressure losses, however this cannot be taken as a certainty and further testing is needed. The results for geometries with 0.25 mm thick walls seemed to present lower heat transfer coefficients with geometry 4 being an exception,
- Both pressure losses and heat transfer coefficients for the intermediate scenario were higher than the ambient temperature scenario and lower than the near saturation scenario. Pressure losses for geometry 2 presented deviations from the theory like those seen for the narrower geometries in the ambient temperature scenario, so these deviations are most likely due to experimental uncertainties.
- The results of this study can provide valuable insights not only for researchers and users but also for those working in electronics and renewable energy devices, as they may lead to potential improvements in the cooling process of microchannel heat sinks.
- Further studies need to be developed with the objective of optimizing the performance of higher velocity flows, especially in the two-phase region because of the cooling requirements of a solar cell.

Declaration of Competing Interest

The authors declare that they have no known competing financial interests or personal relationships that could have appeared to influence the work reported in this paper.

Data availability

Data will be made available on request.

Acknowledgements

Authors acknowledge to Fundação para a Ciência e Tecnologia (FCT) for partially financing the research through project PTDC/EMETED/7801/2020 and UIPD/50009/2020-FCT and UIDB/50009 - FCT to Portuguese Army – Ministério da Defesa, for financing projects CINAMIL STECOMBAT - Development of thermal management and climatization systems for NBQ equipment and COOLUAV – Cooling system for electronics and batteries for military unmanned vehicles, which partially also supported this project. Mr. Pedro Pontes also acknowledges FCT for supporting his PhD fellowship (Ref. SFRH/BD/149286/2019).

References

[1] Flightpath 2050: Europe's vision for aviation: maintaining global leadership and serving society's needs, Publications Office, 2011. https://data.europa.eu/doi/10.2777/50266.
[2] M. Coutinho, D. Bento, A. Souza, R. Cruz, F. Afonso, F. Lau, A. Suleman, F. R. Barbosa, R. Gandolfi, W. Affonso Junior, F. I.K. Odaguil, M. F. Westin, R, J.N. dos Reis, C. R.I. da Silva, A review on the recent developments in thermal management systems for hybrid-electric aircraft, Applied Thermal Engineering 227(2023) 120427. 10.1016/j.applthermaleng.2023.120427.
[3] N. Javani, I. Dincer, G.F. Naterer, B.S. Yilbas, Exergy analysis and optimization of a thermal management system with phase change material for hybrid electric vehicles, Appl. Therm. Eng. 64 (2014) 471–482, https://doi.org/10.1016/j.applthermaleng.2013.11.053.
[4] K. Li, Z. Liu, J. Xu, H. Liu, S. Xu, C. Wang, J. Qin, Evaluation of high-speed aircraft thermal management system based on spray cooling technology: Energy analysis, global cooling, and multi-objective optimization, Appl. Therm. Eng. 229 (2023), 120632, https://doi.org/10.1016/j.applthermaleng.2023.120632.

[5] A. van Heerden, D. Judt, S. Jafari, C. Lawson, T. Nikolaidis, D. Bosak, Aircraft thermal management: Practices, technology, system architectures, future challenges, and opportunities, Prog. Aerosp. Sci. 128 (2022), 100767, https://doi.org/10.1016/j.paerosci.2021.100767.

[6] D.R. Herber, J.T. Allison, R. Buettner, P. Abolmoali, S.S. Patnaik, Architecture generation and performance evaluation of aircraft thermal management systems through graph-based techniques, AIAA Scitech 2020 Forum, 6-10 January 2020 Orlando, FL2020, https://doi.org/10.2514/6.2020-0159.

[7] J.X. Wang, W. G. Kai, X. Sheng, S.N, Wang, Review of aerospace-oriented spray cooling technology, Progress in Airspace Sci 116 (2020):100635. 10.1016/j.paerosci.2020.100635.

[8] M. Yoshida, S. Yamada, Y. Funami, H. Nakamura, High spatio-temporal resolution measurement of boiling heat transfer of a falling droplet, Appl. Therm. Eng. 228 (2023), 120464, https://doi.org/10.1016/j.applthermaleng.2023.120464.

[9] Q. Zhang, Z. Feng, J. Zhang, F. Guo, S. Huang, Z. Li, Design of a mini-channel heat sink for high-heat-flux electronic devices, Appl. Therm. Eng. 216 (2022), 119053, https://doi.org/10.1016/j.applthermaleng.2022.119053.

[10] Manoj, U.V., A.R., Goddumarri, S. Chakraborty, Heat transfer and fluid flow characteristics of a microchannel heat sink with microplates - A critical computational study, Applied Thermal Engineering 226(2023) 120309. 10.1016/j.applthermaleng.2023.120309.

[11] Z. Tan, P. Jin, Y. Zhang, G. Xie, Flow and thermal performance of a multi-jet twisted square microchannel heat sink using CuO-water nanofluid, Appl. Therm. Eng. 225 (2023), 120133, https://doi.org/10.1016/j.applthermaleng.2023.120133.

[12] A. Rajalingam, S. Chakraborty, Effect of shape and arrangement of micro-structures in a microchannel heat sink on the thermo-hydraulic performance, Appl. Therm. Eng. 190 (2021), 116755, https://doi.org/10.1016/j.applthermaleng.2021.116755.

[13] H.A. Kose, A. Yildizeli, S. Cadirci, Parametric study and optimization of microchannel heat sinks with various shapes, Appl. Therm. Eng. 211 (2022), 118368, https://doi.org/10.1016/j.applthermaleng.2022.118368.

[14] R. Kumar, G. Singh, D. Mikielewicz, Effect of asymmetric fluid flow distribution on flow boiling in a microchannel heat sink – An experimental investigation, Appl. Therm. Eng. 213 (2022), 118710, https://doi.org/10.1016/j.applthermaleng.2022.118710.

[15] H. Dai, C. Zhu, Y. Liu, Thermal performance of double-layer porous-microchannel with phase change slurry, Appl. Therm. Eng. 211 (2022), 118457, https://doi.org/10.1016/j.applthermaleng.2022.118457.

[16] C. Li, X. Li, H. Huang, Y. Zheng, Hydrothermal performance analysis of microchannel heat sink with embedded module with ribs and pin-fins, Appl. Therm. Eng. 225 (2023), 120167, https://doi.org/10.1016/j.applthermaleng.2023.120167.

[17] M. Parlak, A. Özsunar, A. Koşar, High aspect ratio microchannel heat sink optimization under thermally developing flow conditions based on minimum power consumption, Appl. Therm. Eng. 201 (2022), 117700, https://doi.org/10.1016/j.applthermaleng.2021.117700.

[18] S. Sabzpoushan, M. Sabouri, Secondary flow through lateral passages to improve hydrothermal performance of liquid-cooled microchannel heat sinks, Appl. Therm. Eng. 227 (2023), 120009, https://doi.org/10.1016/j.applthermaleng.2023.120009.

[19] Dooley, M., Lui, N., Newman, R., and Lui, C., "Aircraft Thermal Management -Heat Sink Challenge," SAE Technical Paper 2014-01-2193, 2014, 10.4271/2014-01-2193.

[20] K. Tan, Y. Hu, Y. He, Enhancement of flow boiling in the microchannel with a bionic gradient wetting surface, Applied Thermal Engineering, In Press 120784 (2023), https://doi.org/10.1016/j.applthermaleng.2023.120784.

[21] P. Smakulski, S. Pietrowicz, A review of the capabilities of high heat flux removal by porous materials, microchannels and spray cooling techniques, Appl. Therm. Eng. 34 (2016) 636–646, https://doi.org/10.1016/j.applthermaleng.2016.05.096.

[22] F. Zhang, L. Zhai, L. Zhang, M. Yi, B. Du, S. Li, A novel hybrid battery thermal management system with fins added on and between liquid cooling channels in composite phase change materials, Appl. Therm. Eng. 207 (2022), 118198, https://doi.org/10.1016/j.applthermaleng.2022.118198.

[23] G. Marseglia, M. Sanches, A.P.C. Ribeiro, A.L.N. Moreira, A.S. Moita, Thermofluid characterization of nanofluids in spray cooling, Appl. Therm. Eng. 210 (2022), 118411, https://doi.org/10.1016/j.applthermaleng.2022.118411.

[24] D. Tuckerman, R.F.W. Pease, High performance heat sinking for vlsi, Electron Device Letters, IEEE 2 (06 1981.), https://doi.org/10.1109/EDL.1981.25367.

[25] T. M. Harms, M. J. Kazmierczak, F. M. Gerner, Developing convective heat transfer in deep rectangular microchannels, International Journal of Heat and Fluid Flow, 20 (2) (199) :149–157. 10.1016/S0142-727X(98)10055-3.

[26] G. Harpole, J. Eninger, Microchannel heat exchanger optimization. Physics, Engineering 1991 Proceedings, Seventh IEEE Semiconductor Thermal Measurement and Management Symposium pages 59-63, 03 1991. ISBN 0-87942-664-0. doi:10.1109/STHERM.1991.152913.

[27] J.H. Ryu, D.H. Choi, S.J. Kim, Three dimensional numerical optimization of a manifold microchannel heat sink, Int. J. Heat Mass Transf. 46 (9) (2003) 1553–1562, https://doi.org/10.1016/S0017-9310(02)00443-X.

[28] X.L. Xie, Z.J. Liu, Y.L. He, W.Q. Tao, Numerical study of laminar heat transfer and pressure drop characteristics in a water-cooled minichannel heat sink, Applied Thermal Engineering 29(1) (200) :64-74. 10.1016/j.applthermaleng.2008.02.002.

[29] D.R.S. Raghuraman, R. Thundil Karuppa Raj, P.K. Nagarajan, B.V.A. Rao. Influence of aspect ratio on the thermal performance of rectangular shaped micro channel heat sink using cfd code. Alexandria Engineering Journal, 56(1) (2017) :43–54, 10.1016/j.aej.2016.08.033.

[30] T.N. Tran, M.W. Wambsganss, D.M. France, Small circular- and rectangular-channel boiling with two refrigerants, Int. J. Multiph. Flow 22 (3) (1996) 485–498, https://doi.org/10.1016/0301-9322(96)00002-X.

[31] J. Lee, I. Mudawar, Fluid flow and heat transfer characteristics of low temperature two-phase micro-channel heat sinks – part 1: Experimental methods and flow visualization results, Int. J. Heat Mass Transf. 51 (2008) 4315–4326, https://doi.org/10.1016/j.ijheatmasstransfer.2008.02.012.

[32] Y. Li, H. Wu, Experiment investigation on flow boiling heat transfer in a bidirectional counter-flow microchannel heat sink. International Journal of Heat and Mass Transfer 187 (2022) :122500, 10.1016/j.ijheatmasstransfer.2021.122500.

[33] W.S. Ling, W. Zhou, C.Z. Liu, F. Zhou, D. Yuan, J.L. Huang, Structure and geometric dimension optimization of interlaced microchannel for heat transfer performance enhancement, Appl. Therm. Eng. 170 (2020), 115011, https://doi.org/10.1016/j.applthermaleng.2020.115011.

[34] M. W. Wambsganss, J. A. . Jendrzejczyk, e D. M. France, Two-Phase flow patterns and transitions in a small, horizontal, rectangular channel, Int. J. Multiph. Flow, 17 (3) (1991) 327–342.

[35] J. Lee e I. Mudawar, Low-temperature two-phase microchannel cooling for high-heat-flux thermal management of defense electronics», IEEE Trans. Components Packag. Technol., 32(2) (2009) 453–465.

[36] W. Li, J. Ma, T. Alam, F. Yang, J. Khan, e C. Li, Flow boiling of HFE-7100 in silicon microchannels integrated with multiple micro-nozzles and reentry micro-cavities», Int. J. Heat Mass Transf., 123 (2018) 354–366.

[37] J. Ma, W. Li, C. Ren, J. A. Khan, e C. Li, Realizing highly coordinated, rapid and sustainable nucleate boiling in microchannels on HFE-7100, Int. J. Heat Mass Transf., 133 (2019) 1219–1229.

[38] T. Harirchian e S. V. Garimella, Effects of channel dimension, heat flux, and mass flux on flow boiling regimes in microchannels, Int. J. Multiph. Flow, 35(4) (2009) 349–362.

[39] S.G. Kandlikar, Heat transfer mechanisms during flow boiling in microchannels, J. Heat Transfer 126 (1) (2004) 8–16.

[40] B. Markal, O. Aydin, M. Avci, Prediction of Heat Transfer Coefficient in Saturated Flow Boiling Heat Transfer in Parallel Rectangular Microchannel Heat Sinks: An Experimental Study, Heat Transfer Engineering, 38(2017):16, 1415-1428, DOI: 10.1080/01457632.2016.1255038.

[41] X. Zhuang, Y. Xie, X. Li, S. Yue, H. Wang, H. Wang, P. Yu, Experimental investigation on flow boiling of HFE-7100 in a microchannel with pin fin array, Appl. Therm. Eng. 225 (2023), 120180, https://doi.org/10.1016/j.applthermaleng.2023.120180.

[42] B. Markal, A. Candan, O. Aydin, M. Avci, Experimental investigation of flow boiling in single microchannels with low mass velocities, Int. Commun. Heat Mass Transfer 98 (2018) 22–30, https://doi.org/10.1016/j.icheatmasstransfer.2018.08.002.

[43] B. Markal, B. Kul, B., Influence of downstream cross-sectional area ratio on flow boiling characteristics of expanding micro pin fin heat sinks. International Communications in Heat and Mass Transfer 143(2023), 106689. 10.1016/j.icheatmasstransfer.2023.106689.

[44] B. Markal, B. Kul, Combined influence of artificial nucleation site and expanding cross section on flow boiling performance of micro pin fins, Int. Commun. Heat Mass Transfer 135 (2022), 106081, https://doi.org/10.1016/j.icheatmasstransfer.2022.106081.

[45] Engineered fluid hfe-7100 physical properties, 2 2002.

[46] E. Teodori, P. Pontes, A.S. Moita, A.L.N. Moreira, Thermographic analysis of interfacial heat transfer mechanisms on droplet/wall interactions with high temporal and spatial resolution, Exp. Therm Fluid Sci. 96 (2018) 284–294, https://doi.org/10.1016/j.expthermflusci.2018.03.013.

[47] J. Mendes, Técnicas de pós-processamento de imagem para métodos experimentais em termografia, Instituto Superior Técnico, 2021. Master's thesis,.

[48] G. Katyba, K. Zaytsev, I. Dolganova, I. Shikunova, N. Chernomyrdin, S. Yurchenko, G. Komandin, I. Reshetov, V. Nesvizhevsky, V. Kurlov, Sapphire shaped crystals for waveguiding, sensing and exposure applications, Prog. Cryst. Growth Charact. Mater. 64 (4) (2018) 133–151, https://doi.org/10.1016/j.pcrysgrow.2018.10.002.

[49] S. Halelfadl, A. Adham, N. Mohd-Ghazali, T. Mare, P. Estelle, R. Ahmad, Optimization of thermal performances and pressure drop of rectangular microchannel heat sink using aqueous carbon nanotubes based nanofluid, Applied Thermal Engineering, 62(2014): 492-499, 01. 10.1016/j.applthermaleng.2013.08.005.

[50] R.K. Shah, A.L. London, Laminar flow forced convection in ducts: a source book for compact heat exchanger analytical data, Academic press, 2014.

[51] R.J. Phillips, Forced-convection, liquid cooled, microchannel heat sinks, Massachusetts Institute of Technology, 1987. PhD thesis,.

[52] W.M. Kays, Convective heat and mass transfer, Tata McGraw-Hill Education, 2011.

[53] D.B.R. Kenning, Y. Yan, Pool boiling heat transfer on a thin plate: features revealed by liquid crystal thermography, Int. J. Heat Mass Transf. 39 (15) (1996) 3117–3137, https://doi.org/10.1016/0017-9310(96)00006-3.

[54] R.J. Moffat, Describing the uncertainties in experimental results, Exp. Therm Fluid Sci. 1 (1) (1988) 3–17, https://doi.org/10.1016/0894-1777(88)90043-X.

[55] K.-S. Yang, Yeau-Ren Jeng, Chun-Min Huang, C.-C. Wang, Heat transfer and flow pattern characteristics for hfe-7100 within microchannel heat sinks, Heat Transfer Engineering 32 (2011) (7-8):697–704. 10.1080/01457632.2010.509774.

[56] L. Martins, Sistema de refrigeração por microcanais com escoamento multifásico para painéis solares de alta concentração, Instituto Superior Técnico, 2020. Master's thesis,.

[57] B.-R. Fu, C.-Y. Lee, C. Pan, The effect of aspect ratio on flow boiling heat transfer of hfe-7100 in a microchannel heat sink, Int. J. Heat Mass Transf. 58 (1) (2013) 53–61, https://doi.org/10.1016/j.ijheatmasstransfer.2012.11.050.
[58] Y.K. Prajapati, M. Pathak, M. K. Khan, Bubble dynamics and flow boiling characteristics in three different microchannel configurations, International Journal of Thermal Sciences, 112(2017:371-382. 10.1016/j.ijthermalsci.2016.10.021.
[59] C. B. Tibiriçá, L.E. Czelusniak, G. Ribatski, Critical Heat flux in a 0.38 mm microchannel and actions for suppression of flow boiling instabilities, Experimental Thermal and Fluid Science, 67(2015):48–56. 10.1016/j.expthermflusci.2015.02.020.
[60] B. Markal, O. Aydin, M. Avci, Effect of aspect ratio on saturated flow boiling in microchannels, Int. J. Heat Mass Transf. 93 (2016) 130–143, https://doi.org/10.1016/j.ijheatmasstransfer.2015.10.024.
[61] S.T. Kadam, R. Kumar, Twenty first century cooling solution: microchannel heat sinks, Int. J. Therm. Sci. 85 (2014) 73–92, https://doi.org/10.1016/j.ijthermalsci.2014.06.013.
[62] S.G. Kandlikar, Mechanistic considerations for enhancing flow boiling heat transfer in microchannels, Journal of Heat Transfer, ASME, 138(2)(2016):021504 (16pages). 10.1115/1.4031648.
[63] C. Dang, L. Jia, Q. Peng, L. Yin, Z. Qi, Comparative study of flow boiling heat transfer and pressure drop of HFE-70 0 0 in continuous and segmented microchannels. International Journal of Heat and Mass Transfer, 148(2020): 11903. Doi: 10.1016/j.ijheatmasstransfer.2019.119038.
[64] X. Cheng, H. Wu, Improved flow boiling performance in high-aspect-ratio interconnected microchannels. International Journal of Heat and Mass Transfer, 165(2021):120627. 10.1016/j.ijheatmasstransfer.2020.120627.